Temperature and Bias Voltage Studies of a Large Area Position Sensitive Avalanche Photodiode

A. Vandenbroucke, J. Lee, V. Spanoudaki, F.W.Y. Lau, P.D. Reynolds, C.S. Levin

***Abstract*—We are constructing a 1 mm^3 resolution, high sensitivity PET detector system with depth of interaction capability. The detectors are built from modules comprising LSO crystal arrays coupled to Position Sensitive Avalanche Photodiodes (PSAPDs). The entire system will have 4,608 densely packed dual LSO-PSAPD modules. The performance of the large area (1x1 cm^2) PSAPDs in our system depends on bias voltage and temperature. Coincidence data was obtained by placing a ^{22}Na source between an LSO crystal coupled to a PMT and an LSO-PSAPD module. The bias voltage was varied between 1695 and 1780 V. The energy resolution remains constant around 14.1 ± 0.01 % (Standard Error - SE) FWHM at 511 keV between 1710 and 1780 V, and decreases by about 5 % when the applied voltage is between 1695 and 1710 V for a specific sample. Crystal identification capability stays constant over the observed range. Optimal coincidence time resolution of 2.63 ± 0.02 ns (SE) FWHM was observed around 1740 V at room temperature. Coincidence time resolution decreases by about 10 % for a 20 V change. The gain increases by a factor of 2 for every 35 Volt increase and can be described by two exponentials. The point where those two exponentials intersect corresponds to the beginning of the avalanche breakdown. The module's temperature was varied using a thermoelectric cooler coupled to a heatsink. In general, decreasing the temperature of a PSAPD improves performance. The coincidence time resolution improved from 5.88 ± 0.05 ns (SE) FWHM at 39°C to 1.96 ± 0.03 ns (SE) at 5 °C. 511 keV energy resolution improved from 14.43 ± 0.01 % (SE) at 39°C to 11.82 ± 0.01 % 5°C. PSAPD gain increases by 25 % every 4.5°C increase. The rate of gain increase is even larger (10 % per degree) at the lowest temperatures. Most of the observed behavior is attributed to the PSAPD, since the light output of LSO varies only slightly with increasing temperature. In summary, we present the performance variation of a large area PSAPD as a function of temperature and bias voltage. These parameters are of extreme importance in densely packed systems needed for state-of-the art PET design.**

***Index Terms*—PET, PEM, PSAPD, scintillation, Depth of Interaction, APD, bias voltage, temperature**

I. Introduction

We are building novel 1 mm^3 resolution, high sensitivity PET scanners for breast [1, 2] and small animal imaging [3]. These systems are designed with a new concept for three dimensional photon positioning intended to provide a uniform intrinsic spatial resolution of 1 mm^3, high scintillation light collection efficiency, and directly measured photon depth of interaction (DOI).

The dual panel breast PET scanner we are developing will be built out of 4,608 dual LSO-PSAPD modules, one of which is depicted on the left side of Fig. 1. Each module consists of two 8×8 arrays of $1 \times 1 \times 1$ mm^3 LSO crystals. Each of these arrays is coupled to two distinct, large area (1×1cm^2) PSAPDs, which are both mounted on the same flex circuit. The PSAPDs each have 5 readout channels, one for the $p-$side and four coupled to the $n-$side over a resistive sheet giving spatial information [4]. The use of a PSAPD enables us to read out 128 crystals with only 10 channels per dual LSO-PSAPD module. This number can be even further reduced by applying a dedicated multiplexing scheme [5]. For this work, the PSAPD is embedded in an Aluminum Nitride (AlN_3) frame providing mechanical strength and electrical isolation.

The PET scanner will be built from many stacks of these LSO-PSAPD modules as indicated in the right side of Fig. 1. 511 keV photons from positron decays will hit the stack 'edge-on', so that an effective thickness of at least 1.6 cm of LSO is provided. Depth of Interaction (DOI) is directly measured by the segmentation of the LSO arrays and the position sensitivity of the PSAPD. The proposed design enables the identification of the annihilation photon interaction locations in all three dimensions.

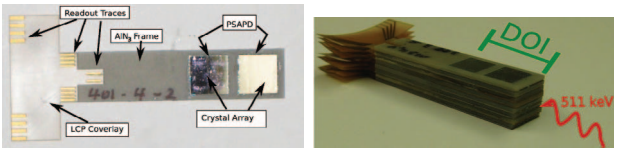

Fig. 1. The left picture shows a top view of one of the dual LSO-PSAPD based detector modules used in the setup. The various parts are indicated in the figure. Right shows a stack of these modules. 511 keV photons enter the detectors 'edge-on', enabling directly-measured photon DOI and high scintillation light collection efficiency.

To build the system, 16 dual LSO-PSAPD modules will be arranged side-to-side into an aluminum registration card, which provides alignment and mechanical strength. Furthermore, the sides of these registration cards will be cooled so that the heat produced by the modules can be effectively dissipated. An imaging head will consist of a stack of many of these cards. Fig. 2 shows the ordering of dual LSO-PSAPD modules into a registration card and the stacking of those cards into an imaging head.

This dense packing of many of these LSO-PSAPD modules in our system requires carefully designed cooling structures.

Manuscript received November 20, 2009. This work was supported by US NIH-NCI grant R01 CA119056-04S109 and NIH-NIBIB R33EB003283, and a post-doctoral fellowship from the Belgian-American Research Foundation.

A. Vandenbroucke and V. Spanoudaki are at the Department of Radiology, Stanford University. F.W.Y. Lau and P.D. Reynolds are at the Department of Radiology and Electrical Engineering, Stanford University. C.S. Levin is at the Departments of Bioengineering, Electrical Engineering and Radiology at Stanford University. J. Lee is at the department of Mechanical Engineering at Stanford University. All authors are associated with the Molecular Imaging Program at Stanford.

Corresponding author: arnevdb@stanford.edu

One LSO-PSAPD module, biased to 1740 V, produces about 2 mW of power. In addition, the readout electronics in the back of the system produce about 200 W of heat. The proposed cooling from the sides of the registration cards will result in a temperature gradient in the system. Preliminary simulations showed a gradient of about $4°$C across the registration cards [2]. This paper shows the performance dependence of an LSO-PSAPD module as a function of temperature, and at the same time we investigate the influence of bias voltage on the performance of the LSO-PSAPD modules.

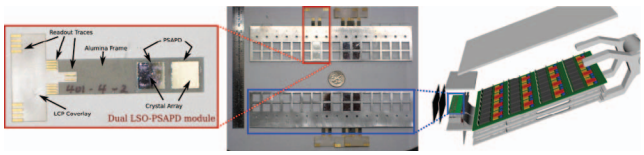

Fig. 2. Schematic of the construction of an imaging head: dual LSO-PSAPD modules (on the left) will be arranged into registration cards (center) which will be stacked to form an imaging head (right). The readout electronics located in the imaging head are drawn as well. The coin in the center is an indication of the dimensions.

II. Methods

All data presented was obtained using a ^{22}Na point source. To obtain coincidence timing information, a $1 \times 1 \times 1\text{cm}^3$ LYSO block was connected to a Hamamatsu H3164 Photo Multiplier Tube (PMT) using optical grease (BICRON BC 630) and Teflon tape. As depicted in Fig. 3, the ^{22}Na point source was positioned in between the LSO-PSAPD detector module and the LYSO-PMT detector. The height of the source was adjusted to assure that every 1 mm^3 crystal receives about the same number of 511 keV photons.

The PSAPD's charge output was amplified using a charge sensitive preamplifier (CR-110 by CREMAT). The signal from the preamplifier was fed into an ORTEC-855 spectroscopy amplifier, whose shaping time was set to 500 ns. The latter output was connected to a National Instruments ADC (NI PCI-6110) , after passing through an ORTEC-427A delay amplifier. The PMT's output was amplified as well and lead into the ADC.

Timing information was obtained by the PSAPD's common (p-side) signal, which was also preamplified by a CR-110 from CREMAT, and further shaped by a fast filter amplifier (ORTEC-579). An ORTEC 935 constant fraction discriminator (CFD) was used to discriminate noise and to mitigate time walk. The PMT's output was fed directly into the same CFD, and served as a start signal for the ORTEC 567 time to amplitude converter (TAC). A variable fine delay (ORTEC 425A) between the PMT's output and the TAC accounted for calibration of the TAC. The signal of the PSAPD's common signal served as a stop signal for the TAC. Because of the large delay used in the CFD for the PSAPD's common, no additional delay was necessary for the TAC's stop signal. The CFD threshold for both PMT and PSAPD were set well below the Compton edge but above the noise floor. One of the TAC's output went into the ADC, the other into a gate generator (ORTEC 416A) serving as a trigger for the ADC unit. A schematic of the setup is shown in Fig. 3.

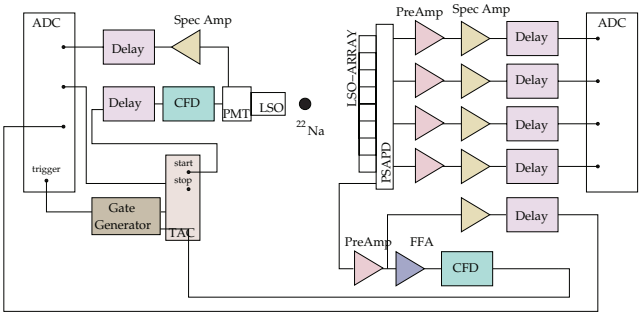

Fig. 3. Schematic overview of the setup and electronics used in the measurements. The drawing is not to scale.

For the temperature dependence studies, the LSO-PSAPD module was placed in a sealed container schematically depicted in Fig. 4. Dry air was blown in the container to prevent moisture from condensing on the modules. The temperature was modified by changing the current to a thermoelectric (Peltier) cooler positioned between the module and a heat sink. In order to achieve temperatures above and below the ambient temperature, the polarity of the supply to the peltier cooler was reversed. The temperature was measured by a thermocouple wire connected to the AlN_3 frame enclosing the LSO-arrays and touching the outer edge of the PSAPDs. AlN_3 is a thermal conductor and therefore we assumed it to be in equilibrium with the temperature of the PSAPDs.

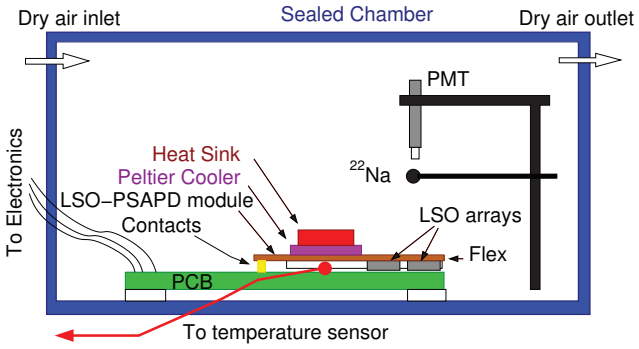

Fig. 4. Schematic of the cooling setup. The sketch is not to scale.

As an indication of uniform irradiation, Fig. 5 shows a flood histogram at room temperature and bias voltage of -1735 Volt. All 64 individual crystals are clearly identified.

For each individual crystal, we determined gain, energy and time resolution. Gain was assessed by the 511 keV photopeak location and energy resolution by the ratio of the FWHM of the 511 keV photopeak spectrum to the photopeak position. Coincidence time resolution was estimated from the FWHM of the TAC spectrum at 511 keV.

Fig. 6 shows the typical gain, energy and time resolution at $22.6°$C for each crystal in the array. The average value is indicated by the red line in the figure, the shaded box demonstrates the standard deviation. No systematic effects across the array are seen. We measure an average gain of $7.37 \pm 0.23\ V$, an average energy resolution of 13.5 ± 0.6 % FWHM, and an average time resolution of 2.9 ± 0.2 ns. The quoted error bars here are RMS standard deviation.

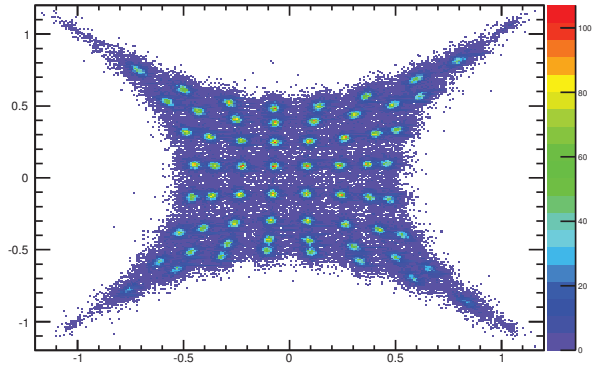

Fig. 5. Flood histogram of an 8×8 array coupled to a PSAPD.

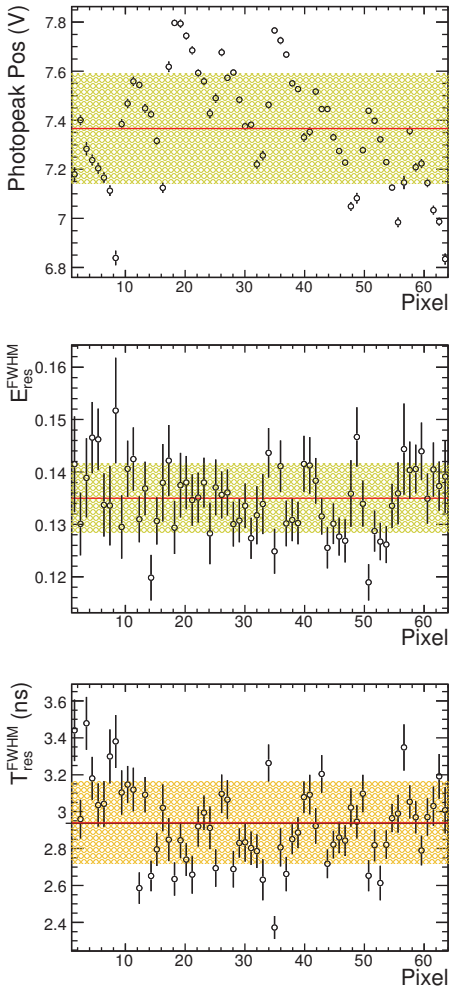

Fig. 6. Gain, energy and time resolution for all crystals of an 8×8 array. Data obtained at $22.6°$C.

In order to assess the crystal identification capability, a figure of merit was introduced for a profile through the crystals seen in the flood histogram:

$$\text{FOM} = \frac{\text{Average distance between the peaks}}{\text{FWHM of the peaks}}.$$

This FOM was calculated for a top and a center row. Fig. 7 shows an example of a top and a center profile histogram through the flood spectrum. The pincushion apparent in Fig. 5 is reflected in the figure.

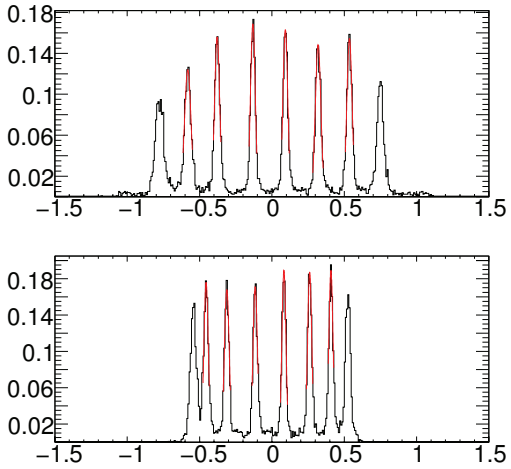

Fig. 7. Profile histogram through the flood of Fig. 5 for a top (top) and bottom (bottom) row. Each peak position is normalized to one.

III. Results

Fig. 8 shows the performance variation as a function of temperature. Error bars in the figure are standard error (SE). The previously mentioned gain, energy and coincidence time resolution at $22.6°$C can easily be determined in the figure. We see that the gain increases exponentially with decreasing temperature. An exponential function was fit to the data. Fit parameters are indicated in the figure and indicate that the PSAPD gain increases by about 25 % every 4.5 degrees. At temperatures below about $8°$C, the gain deviates from the fitted exponential.

The energy resolution remains constant between $10°$C and $30°$C. At lower (higher) temperatures the energy resolution improves (degrades). The coincidence time resolution improves at lower temperatures. A third order polynomial was fit to the data, and we see that the increase in time resolution has a less than exponential dependence on temperature. Also crystal identification improves at lower temperatures as observed from the FOM.

Another important observable which may vary as a function of temperature is the location of the peak crystal intensity in the flood histogram. Fig. 9 shows the peak locations for different temperatures. A compression in crystal peak locations at lower temperatures can be observed. This compression is probably caused by preamplifier saturation due to a higher gain at lower temperatures for events occurring at the corner. Saturation only occurs for these corner events since we do not observe similar compression at the center rows and columns.

The light output of LSO is also dependent on temperature. Reference [6] claims a decreased light output of 25 % between 275 K ($\sim 2°$C) and 310 K ($\sim 35°$C) for LSO, while [7] reports a decrease between 8 % and 37 % depending on the Cerium concentration. Within the temperature range discussed

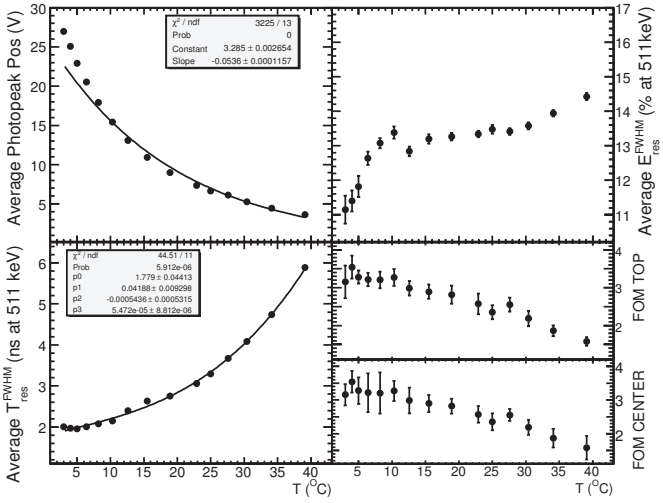

Fig. 8. Performance variation as a function of temperature. Upper left shows the average gain, lower left the average FWHM coincidence time resolution, upper right the average energy resolution (FWHM at 511 keV), middle right the FOM for a top row, and lower right the FOM for a center row.

in this paper, the scintillation light variations are low. Moreover, the investigation presented here aims at evaluating the performance of the combined LSO-PSAPD module.

Apart from the varying light output of the scintillation crystal, its emission spectrum may also shift towards shorter wavelengths at lower temperatures. This effect was for instance observed in the LabPET system [8] where the LGSO's emission spectrum establishes a temperature dependent wavelength shift. The LYSO's output in the same scanner (LabPET) does not have such a temperature dependence [9],

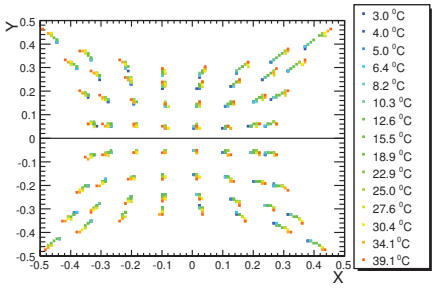

Fig. 9. Peak crystal intensity location in the flood histogram for different temperatures.

The performance as a function of bias voltage is depicted in Fig. 10. The gain increases when increasing the bias voltage, and the behavior can be described by two exponentials. The fit parameters of both exponentials are indicated in the figure. From these we conclude that the gain increases by 25% every 12 Volt (8.5 Volt) for the lower (higher) bias voltages. The two exponentials overlap at 1742 V.

The same figure shows that the energy resolution stays constant over the observed range, while the coincidence time resolution establishes a distinct minimum between 1730 and 1760 V. The coincidence time resolution was fit by a third order polynomial. The FOM seems to be optimal between 1720 and 1770 V for both the top and the bottom row. The absolute values of the FOM are different than in Fig. 8, since a different crystal array was used: for the temperature measurements we were using a crystal array without inter-crystal reflectors, for the bias voltage dependence measurement, an array with inter-crystal reflector was used. What is important here is the relative variation observed as a function of the operating condition. More details about the crystal configuration can be found in [10].

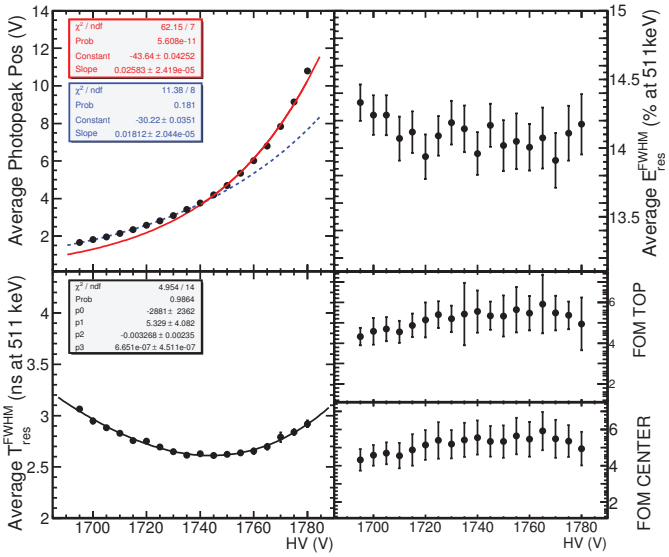

Fig. 10. Performance variation as a function of bias voltage. Upper left shows the average gain, lower left the average FWHM coincidence time resolution, upper right the average energy resolution (FWHM at 511 keV), middle right the FOM for a top crystal row, and lower right the FOM for a center row.

Looking at the location of the peak crystal intensity in the flood histogram, Fig. 11, no variation is observed. We consequently can adjust the bias voltage without penalty in the flood histogram peak location. Thus, assigning crystal positions to individual events is independent of the bias voltage.

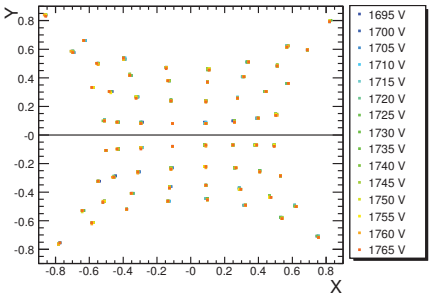

Fig. 11. Peak crystal intensity location in the flood histogram for different bias voltages across the PSAPD.

IV. Discussion

As expected we see an improved performance at lower temperatures. This is due to the fact that at lower temperatures lattice vibrations are less apparent, which causes charge carriers to have a larger mean free path, and thus lose less

energy to lattice phonons [11]. This is also reflected in higher electron and hole mobilities at lower temperatures [12, 13]. The band gap (E_g), however, increases at lower temperatures, due to a shift in the relative position of the conduction and valence bands [14]. The band gap dependence causes the average energy to create an electron-hole pair, ϵ, to increase with decreasing temperature. Indeed, [15] reports a relation: $\epsilon = 2.15 \cdot E_g(T) + 1.2$. The band gap is quadratically dependent on the temperature according to [14]. The electron and hole mobility dependence [12], however, outweighs the bandgap dependence. The combined effect of a higher carrier mobility and a wider bandgap is that of an increased gain at lower temperatures.

The higher gain at lower temperatures also decreases the breakdown voltage as a function of temperature. Fig. 12 shows the leakage current as a function of bias voltage for 5 different temperatures. The steep increase in leakage current at about 1710 and 1720 V for $0.2°$C and $7.2°$C respectively in the figure is an indication of breakdown. The same figure suggests breakdown around 1730 V at $13.6°$C, and no clear evidence of breakdown at $22.6°$C and $35.8°$C.

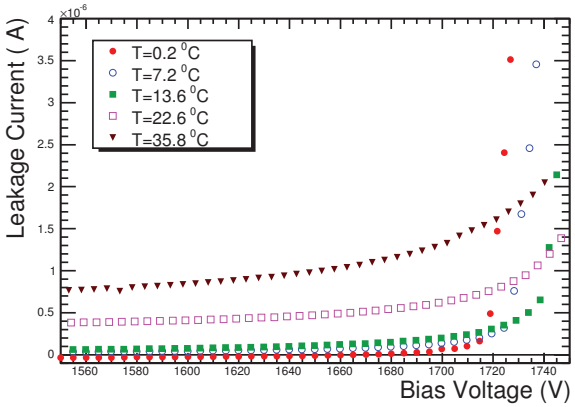

Fig. 12. Leakage current as a function of bias voltage for 5 different temperatures.

The bias voltage dependence measurements depicted in Fig. 10 suggest that the optimal bias voltage for the PSAPDs is around the region where the two exponential intersect. Indeed, it is known that an APD's optimal performance happens just below breakdown, as it gives optimal signal to noise ratio. The red exponential in the top left of Fig. 10 describes the regime of quenched breakdown. We call the breakdown quenched, since the leakage current still goes up with bias voltage. At the same time, the deviation from the exponential fit below about $5°$C in Fig. 8 top left now can also be explained: below $5°$C the module is operating in quenched breakdown mode and hence the gain does not follow the original exponential behavior, but changes more drastically as a function of temperature.

V. Conclusion

This paper presents the temperature and bias voltage dependence of dual LSO-PSAPD modules which we plan to use in a dedicated PET breast camera. At room temperature and optimal bias voltage, an energy resolution of $14.4 \pm 0.01\%$ (SE) FWHM is observed together with a coincidence time resolution of 2.63 ± 0.02 ns (SE) for a specific sample. We have confirmed that the performance deteriorates with increasing temperature. Without any temperature regulation or compensation in our breast PET camera, a degraded performance will be evident. Therefore, a dedicated implementation of temperature regulating structures will be mandatory.

Our measurements indicate that optimal performance is achieved just below breakdown. Breakdown itself is a function of temperature. We showed an optimal performance over a window of about 25 V. The data presented in this paper thus shows that adjusting the bias voltage can compensate for small temperature drifts. The data suggests furthermore that the optimal bias voltage can be determined by analyzing the gain change as a function of bias voltage.

The bias voltage dependence also shows that the coincidence time resolution is the parameter which depends strongest on the applied bias voltage. Coincidence time resolution however is experimentally harder to assess and especially takes longer than the acquisition of single events for a large number of detectors. By identifying the intersection of the two exponential curves describing the gain, we may be able to identify the optimal bias voltage in a much simpler way.

A cross study where the gain is optimized at every temperature is planned as a follow up for the measurements presented here. In addition, we want to investigate whether we can decrease the bias voltage at lower temperatures, thus keeping the gain constant, and still have a similar performance.

References

[1] J. Zhang, P. D. Olcott, G. Chinn, A. M. Foudray, and C. S. Levin, "Study of the Performance of a Novel 1 mm Resolution Dual-Panel PET Camera Design Dedicated to Breast Cancer Imaging Using Monte Carlo Simulation," *Med. Phys*, vol. 34(2), pp. 689–702, 2007, .

[2] F. W. Y. Lau *et al.*, "A 1 mm^3 Resolution Breast Dedicated PET system," in *Proc. IEEE NSS-MIC*, 2008, pp. 5619–5622.

[3] A. Foudray, "Design of an Advanced Positron Emission Tomography Detector System and Algorithms for Imaging Small Animal Models of Human Disease," PhD Thesis, University of California, San Diego, 2008.

[4] K. S. Shah, R. Farrell, R. Grazioso, E. S. Harmon, and E. Karplus, "Position-Sensitive Avalanche Photodiodes for Gamma-Ray Imaging," *IEEE TNS*, vol. 49, pp. 1687–1692, 2002.

[5] F. W. Y. Lau, A. Vandenbroucke, P. D. Reynolds, P. D. Olcott, M. A. Horowitz, and C. S. Levin, "Front-end Electronics for a 1 mm^3 Resolution Avalanche Photodiode Based PET System with Analog Signal Multiplexing," in *Proc. IEEE NSS-MIC*, 2008, pp. 3871–3874.

[6] Y. Chen, B. Liu, C. Shi, G. Ren, and G. Zimmerer, "The Temperature Effect of LU_2SiO_5:Ce^{3+} Luminescence," *Nucl. Instr. Meth.*, vol. A537, pp. 31–35, 2005.

[7] J. D. Naud, T. A. Tombrello, C. L. Melcher, and J. S. Schweitzer, "The Role of Cerium Sites in the Scintillation Mechanism of LSO," *IEEE Transactions on Nuclear Science*, vol. 43, pp. 1324–1328, 1996.

[8] R. Fontaine *et al.*, "The Architecture of LabPET^{TM}, a Small Animal APD-Based Digital PET Scanner," in *Proc. IEEE NSS-MIC*, 2005, pp. 2785–2789.
[9] R. Fontaine, "Dept. of Electr. & Comput. Eng., Sherbrooke Univ., Quebec," private communciation.
[10] A. Vandenbroucke and C. S. Levin, "Array Parameters for an Advanced PET Scanner Dedicated to Breast Cancer Imaging," in *Proc. IEEE NSS-MIC*, 2008, pp. 4914–4919.
[11] C. R. Crowell and S. M. Sze, "Temperature Dependence of Avalanche Multiplication in Semiconductors," *Applied Physics Letters*, vol. 9, no. 6, pp. 242–244, 1966.
[12] N. D. Arora, J. R. Hauser, and D. J. Roulston, "Electron and Hole Mobilities in Silicon as a Function of Concentration and Temperature," *IEEE Trans. Electron Devices*, vol. 29, pp. 292–295, 1982.
[13] S. N. Mohammada, A. V. Bemisb, R. L. Carterc, and R. B. Renbeckd, "Temperature, Electric Field, and Doping Dependent Mobilities of Electrons and Holes in Semiconductors," *Solid-State Electronics*, vol. 36, pp. 1677–1683, 1993, .
[14] Y. P. Varshni, "Temperature Dependence of the Energy Gap in Semiconductors," *Physica*, vol. 34, pp. 149–154, 1967.
[15] C. Canali, M. Martini, G. Ottaviani, and A. A. Quaranta, "Measurements of the Average Energy Per Electron-Hole Pair Generation in Silicon between 5-320K," *IEEE TNS*, vol. 19, pp. 9–19, 1972.